

Mossbauer Spectroscopy of ^{57}Fe

Dennis V. Perepelitsa*
 MIT Department of Physics
 (Dated: April 6, 2007)

Using recoilless Mossbauer spectroscopy methods, we investigate the atomic absorption spectra of the 14.4keV transition in ^{57}Fe compounds. The natural linewidth of this transition is determined to the correct order of magnitude with $\chi^2_\nu = .75$. Hyperfine energy shifts in iron oxide and iron sulfate are investigated and measured. The ratio of ground and excited state magnetic moment in ^{57}Fe is found to be $-1.73(2)$. The internal magnetic field in metallic iron is found to be 350(2) kG. The phenomenon of relativistic time dilation is confirmed with $\chi^2_\nu = 1.52$.

1. INTRODUCTION

In 1958, Rudolf Mossbauer devised a method that allowed the phenomenon of practical *resonance absorption* to occur. Using this method, absorption spectroscopy become possible at a much higher resolution than was otherwise available at the time. Within the next several years, scientists investigated the details of several atomic spectra, measuring hyperfine splitting effects and other values with heretofore unrealizable accuracy.

In this experiment, we probe the absorption spectra of the 14.4 keV line of species containing ^{57}Fe .

2. THEORY

Mossbauer [1] presents how to achieve the phenomenon of resonance absorption by fixing the emission source in a crystal lattice and moving it gently with respect to the absorption source. The first order approximation of the new energy E' given velocity v is given by the Doppler effect:

$$E' = E_0 \left(1 + \frac{v}{c}\right) \quad (1)$$

The *natural linewidth* of an absorption line reflects a fundamental quantum property of incoming radiation - the uncertainty in the energy is tied to the uncertainty in the lifetime of the excited state through Heisenberg's relation: $\Delta E \Delta \tau = \hbar/2$. The spectral line has a Lorentzian profile centered on E_0 with intensity I_0 and full-width half-maximum (FWHM) Γ :

$$L(E) = \frac{I_0 \left(\frac{\Gamma}{2}\right)^2}{(E - E_0)^2 + \left(\frac{\Gamma}{2}\right)^2} \quad (2)$$

Of course, both the emission and absorption line have the above profile, with intensities I_0 and σ_0 , respectively. To model the observed absorption spectrum after it has

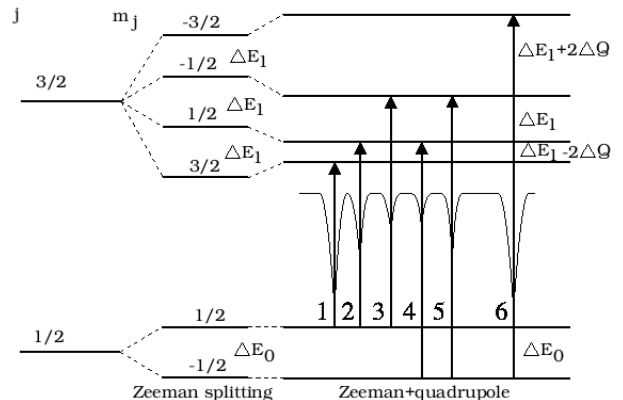


FIG. 1: Left to right: energy level diagram of the 14.4 keV $\frac{3}{2} \rightarrow \frac{1}{2}$ iron-57 transition, split by the Zeeman effect, altered by the electric quadrupole interaction. Significantly modified from <http://www.cmp.liv.ac.uk/>

passed through an absorber of width x , we use the following equation in [2]. Below, A and N are the atomic weight of iron-57 and Avogadro's number, respectively.

$$C(v) = \eta \int_0^\infty L(E) e^{-\frac{\sigma_0 \left(\frac{\Gamma}{2}\right)^2 \frac{N}{A} x}{(E[1+\frac{v}{c}] - E_0 - \Delta C)^2 + \left(\frac{\Gamma}{2}\right)^2}} dE \quad (3)$$

2.1. Hyperfine interactions

Three physical phenomena contribute to the number, location and width of observed absorption peaks.

Under the influence of a magnetic field, such as that exhibited internally by iron in some compounds, *Zeeman splitting* of the energy levels according to total angular momentum number j occurs. Following [3], we report nuclear magnetic moments as multiples of the nuclear magneton μ_N . The energy shift from the original energy level E_i is, for a given angular number m_j and state i is given in [4]:

$$\Delta E(j, i) = -\mu_i B_0 = -\left(\frac{g_i \mu_N I}{\hbar}\right) B_0 = -g_i \mu_N m_j B_0 \quad (4)$$

*Electronic address: dvp@mit.edu

Where μ_i is the *magnetic moment*, expressed as a fraction g_i of the *nuclear magneton* $\mu_N = 3.15 \times 10^{-12}$ eV/gauss, and B_0 is the magnetic field of the nucleus. Since m_j comes in multiples of one-half, the observed spacing between two energy levels with different m_j numbers will some integer multiple of $g_i \mu_N B_0$.

The *quadrupole interaction* is caused by an electric quadrupole moment in the atomic crystal lattice. The ground state of the atom is not affected, but the first excited state is split into sublevels that correspond to different magnitudes of m_j . Let q be the gradient of the electric potential and e^2Q the quadrupole moment. The energy shift ΔQ for the $m_j = \pm\frac{3}{2}$ sublevels (the $m_j = \pm\frac{1}{2}$ energy shift has the same magnitude but opposite sign) is given in [5]:

$$\Delta Q = \frac{qe^2Q}{4j(2j-1)} [3m_j^2 - j(j+1)] = \frac{1}{4}qe^2Q \quad (5)$$

An energy diagram of combined Zeeman splitting and quadrupole-interaction is given in Figure 1.

The *chemical isomer shift* is caused by a difference in chemical environment between source and absorber. It has the effect of shifting all energies by a small amount. A more detailed description is given in [5].

2.2. Relativistic effects

The ^{57}Fe atoms in the lattice oscillate at higher frequencies in at higher temperatures, leading to an energy shift of the accompanying absorption peak from the Doppler effect. The first-order Doppler effect, which replicates the classical one, negates itself in the aggregate. Theoretically, however, the second-order term contributes to a general energy shift. From [6], in the classical limit, the temperature dependence of this shift ΔE_T is

$$\frac{d}{dT} \frac{\Delta E_T}{E} = -\frac{3k}{2Mc^2} \quad (6)$$

3. EXPERIMENTAL SETUP

The heart of our setup is the ASA-S700A Mossbauer Drive Module which drives a ^{57}Co source connected to the end of a piston. ^{57}Co decays by beta capture to ^{57}Fe in an excited state, which emit 14.4keV gamma rays through atomic de-excitation directed at a proportional counter. The piston is moved periodically as a sawtooth function of time by the drive circuit, and the desired absorption source is placed between it and the counter. The counter is connected in series to a high-voltage discriminator and signal amplifier, which directs DC voltage pulses to a central multi-channel scaler (MSC) that vary linearly with the observed amount of counts.

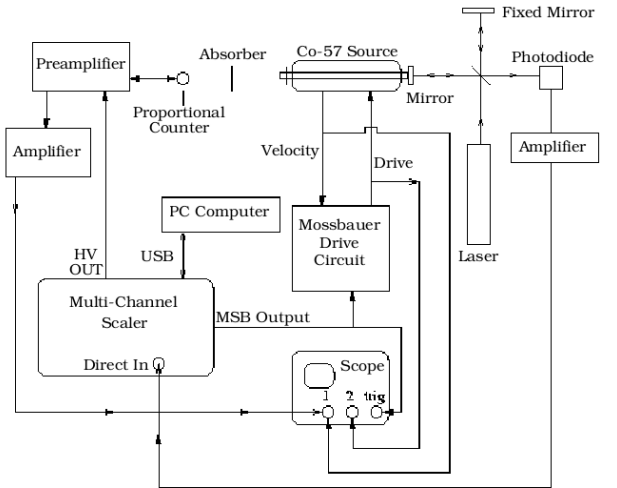


FIG. 2: Piston-mounted decay source and associated absorption spectrum measurement chain with adjacent laser interferometry setup for velocity calculation.

The MSC setup directs the Mossbauer Drive Module and receives the amplified voltage pulses, which is sends to a personal computer for display and analysis. The piston is driven at a frequency of 6Hz and integrated count times over 1024 sweeps of $T \approx 200\mu\text{s}$. To analyze signal stability, the velocity and drive of the MDM was displayed on a digital oscilloscope, and triggered by the rising edge of the MSC.

An adjacent interferometer setup with a laser of wavelength $\lambda = 632.8\text{ nm}$ detailed in Figure 2 determines the velocity of the piston at any given time. Consider the i^{th} channel of the MCS. In the integration time T , the path taken by the beam reflecting off the piston travels a distance $2TV_i$. At each full wavelength of interference, the photodiode records a count. If the cycle is repeated N times and C_i total counts recorded, the velocity of that channel is $V_i = \frac{C_i \lambda}{2NT}$. The output of the photodiode is amplified and replaces the input from the proportional counter during calibration runs.

3.1. Methodology

Before an energy spectrum reading, we attempted to take a velocity calibration using the interferometer setup described above. Due to equipment problems on some days, we calibrated the energy spectrum using the two outer or inner peaks of the metallic iron absorption spectrum.

The Drive Module maximum piston velocity was set to 80mm/s for most spectra, and 10mm/s when taking the sulfate and temperature-dependent data. The fidelity knob was manually adjusted each time to yield a crisp velocity curve. After activating the piston motor, we waited a sufficient time to allow the velocity signal to stabilize before performing a reading. In all cases,

TABLE I: Measured atomic transition energies in enriched metallic iron and iron oxide.

Transition	^{57}Fe	Fe_2O_3
$3/2 \rightarrow 1/2$	$-2.79 \pm .01 \times 10^{-7}$ eV	$-4.17 \pm .01 \times 10^{-7}$ eV
$1/2 \rightarrow 1/2$	$-1.62 \pm .01 \times 10^{-7}$ eV	$-2.20 \pm .01 \times 10^{-7}$ eV
$-1/2 \rightarrow 1/2$	$-0.41 \pm .01 \times 10^{-7}$ eV	$-.41 \pm .01 \times 10^{-7}$ eV
$1/2 \rightarrow -1/2$	$0.40 \pm .01 \times 10^{-7}$ eV	$.86 \pm .01 \times 10^{-7}$ eV
$-1/2 \rightarrow -1/2$	$1.57 \pm .01 \times 10^{-7}$ eV	$2.61 \pm .01 \times 10^{-7}$ eV
$-3/2 \rightarrow -1/2$	$2.68 \pm .01 \times 10^{-7}$ eV	$4.30 \pm .01 \times 10^{-7}$ eV

we recorded absorption spectra until the low absorption peaks and background noise differed by several hundred counts.

To determine the natural line width of enriched iron-57, we recorded the absorption spectra of sodium ferrocyanide ($\text{Na}_3\text{Fe}(\text{CN})_6$) for widths of 0.1, 0.25 and 0.5 mg/cm². Hyperfine interactions were observed in the absorption spectra of metallic iron (enriched ^{57}Fe), iron oxide (Fe_2O_3) and iron sulfates ($\text{Fe}_2(\text{SO}_4)_3$ and $\text{Fe}(\text{SO}_4)$). Finally, we placed a metallic iron sample in a resistance heater and recorded its absorption spectra at four values of the temperature.

4. DATA ANALYSIS

4.1. Natural linewidth of ^{57}Fe

We make two fundamental simplifying assumptions when manipulating (3). We estimate that it can be approximated with a Lorentzian profile, and that the measured full-width of the peak will, when extrapolated linearly, give the natural linewidth. Plotting the full-width half-maximum against absorber thickness and computing the $\chi^2_\nu = .75$ least-squares linear fit, we obtain the linewidth intercept at zero thickness to be $(1.2 \pm .1) \times 10^{-8}$ eV.

4.2. Zeeman splitting in enriched ^{57}Fe

A non-linear fit with $\chi^2_\nu = 1.19$ to the data using Poisson uncertainties (with the consequence that the bottom of the absorption peaks were more heavily weighted) using six Lorentzian profiles and a background distribution was obtained. The data is displayed in Table I. As expected, the average of the two central peaks coincides with the zero velocity value to within the derived uncertainty.

To find the ground state energy split ΔE_0 , we take the weighted average [7] of the differences between transitions from different ground state sublevels to the same excited state sublevels. We use a similar method to determine

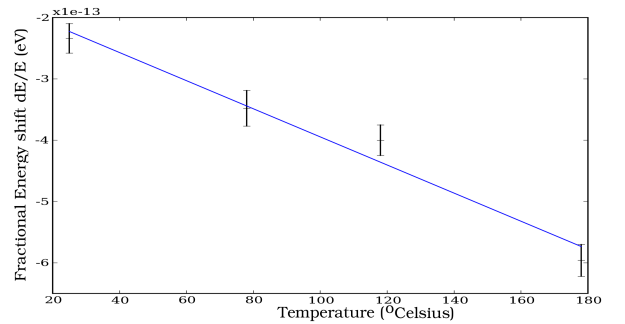


FIG. 3: Plot of fractional energy shift against temperature.

ΔE_1 . The results are

$$\begin{aligned} \Delta E_0 &= (1.99 \pm .01) \times 10^{-7} \text{ eV} \\ \Delta E_1 &= -(1.15 \pm .01) \times 10^{-7} \text{ eV} \end{aligned} \quad (7)$$

From these facts, (4) and the established value of μ_0 in [3], we can calculate ratio of the ground state and first excited state magnetic moment and the internal magnetic field. Our results are summarized in Table II.

4.3. Hyperfine interactions in Fe_2O_3

A similar fitting process resulted in the data in Table I. As indicated in Figure 1, we must account for an additional quadrupole shift ΔQ in the excited substates. Using linear combinations of the transition energies, we can derive the following values:

$$\begin{aligned} \Delta E_0 &= (3.04 \pm .01) \times 10^{-7} \text{ eV} \\ \Delta E_1 &= -(1.78 \pm .01) \times 10^{-7} \text{ eV} \\ \Delta Q &= -(7.0 \pm .2) \times 10^{-9} \text{ eV} \end{aligned} \quad (8)$$

There are several interesting features here. The energy shifts are larger than those in metallic iron by a factor of $(1.53 \pm .02)$, and correspond to an increased internal magnetic field. The ratio of ground and excited state magnetic moments remains the same, within error. The quadrupole shift is in the opposite direction as illustrated in Figure 1, and this leads to a negative value for the product of the field gradient and quadrupole moment $qe^2Q = -(2.8 \pm .01) \times 10^{-8}$ eV. Finally, we calculate the (off-center energy) chemical shift ΔC between metallic iron and Fe_2O_3 . Our results are summarized in Table II.

4.4. Hyperfine interactions in FeSO_4 and $\text{Fe}_2(\text{SO}_4)_3$

Examination of the spectra revealed that FeSO_4 exhibited a quadrupole splitting of the first excited state, while Fe_2SO_4 did not. The quadrupole and chemical shifts are detailed in Table II.

TABLE II: Summary of experimental results. The horizontal linebreaks correspond to separations between different species. They are, in order: metallic iron, iron oxide, iron (II) sulfate and iron (III) sulfate.

Property	Derived Value	Expected Result	Deviation
Γ	$1.2(1) \times 10^{-8}$ eV	$4.7(1) \times 10^{-9}$ eV	-
$\frac{d}{dT} \frac{\Delta E_T}{E}$	$-2.29(22)$ $\times 10^{-15}$ eV·K ⁻¹	$-2.09(6)$ $\times 10^{-15}$ eV·K ⁻¹	$\leq 1\sigma$
μ_0/μ_1	$-1.73(2)$	$-1.75(1)$	$\leq 1\sigma$
B_0	$351(2)$ kG	$330(2)$ kG	6%
μ_0/μ_1	$-1.71(2)$	$-1.77(2)$	$\leq 3\sigma$
B_0	$534(2)$ kG	$513(2)$ kG	4%
ΔQ	$7.0(2) \times 10^{-9}$ eV	$5.7(1.4) \times 10^{-9}$ eV	$\leq 1\sigma$
ΔC	$2.8(1) \times 10^{-8}$ eV	$2.25(14) \times 10^{-8}$ eV	$\leq 4\sigma$
ΔQ	$6.2(1) \times 10^{-8}$ eV	$6.7(2) \times 10^{-8}$ eV	$\leq 3\sigma$
ΔC	$1.60(7) \times 10^{-7}$ eV	$1.54(2) \times 10^{-7}$ eV	$\leq 1\sigma$
ΔC	$2.2(1) \times 10^{-8}$ eV	$2.6(2) \times 10^{-8}$ eV	$\leq 2\sigma$

4.5. Temperature Coefficient of ⁵⁷Fe

Plotting the off-center energy shift against temperature and computing the $\chi^2_\nu = 1.53$ least-squares linear fit, we obtain the temperature dependence $\frac{d}{dT} \frac{\Delta E_T}{E} = -(2.29 \pm .22) \times 10^{-15}$ eV·K⁻¹. This is shown in Figure 3.

5. ERROR ANALYSIS

After calibrating the energy spectrum from the velocity curve, the discrete channel uncertainty due to binning was 1.2×10^{-9} eV. Due to this, we truncate the granularity of all final results to a resolution of 10^{-9} eV. Since the emission and absorption of gamma radiation are nuclear events, we model the channel count uncertainty using Poisson statistics. The error in the independent variable (energy) is thus much smaller than that in the dependent variable (counts), and we do not incorporate it. In our analysis, we do not attempt to model uncertainty in the recorded temperature.

We fit every absorption spectrum after this calibration

using a standard non-linear gradient descent method. Our reduced-chi-squared values ranged from 1.0 to 1.5 and indicated appropriate fits and correctly modeled error. The principal source of error was thus fitted parameter uncertainty, added in quadrature with the energy uncertainty. In the case of most measured energy values, this was on the order of 1%, and higher for derived values.

When forced to perform an energy calibration using other energy spectra as a reference, we fit to find the positions of the reference peak, and assign them energy values we derived earlier. The calibration energy error is then added in quadrature to the parameter found by fitting.

6. CONCLUSIONS

Table II gives a summary of our results. The expected values are drawn from [5], [8] and [3].

There are several complicating factors in our attempt to measure the width of the 14.4 keV line. Doppler smearing of the absorption line from the thermal excitation of the source, and the imperfect resolution of the proportional counter both contribute to the widening of the line. We will have to be satisfied with the fact that our data is of the correct order of magnitude.

Our experimental results concerning hyperfine interactions in metallic iron, iron oxide and iron sulfate are in good agreement with established values, with a caveat. On a qualitative level, we have confirmed the presence of absence of several hyperfine interaction phenomena. Iron (III) exhibits a spherically symmetric charge distribution around the nucleus, while iron (II) does not. Metallic iron and iron oxide possess an internal atomic magnetic field, while ferrocyanide and the sulfates do not.

Quantitatively, many of our measured energy values seem to be systematically higher by approximately 5%. This seems to imply a consistent energy miscalibration, and a topic for further investigation.

The temperature dependence of the energy shift has been confirmed with $\chi^2_\nu = 1.53$. This term cannot be explained under any classical model, and is a confirmation that quickly moving particles exhibit time dilation as predicted by special relativity.

-
- [1] R. Mossbauer, *Nobel lecture* (1961).
[2] J. L. Staff, *Mössbauer spectroscopy*, URL <http://web.mit.edu/8.13/www/JLEperiments/JLExp13.pdf>.
[3] R. Preston, S. Hanna, and J. Heberle, *Phys. Rev. Lett.* **128** (1962).
[4] D. J. Griffiths, *Introduction to Quantum Mechanics* (Pearson Prentice Hall, 2005), 2nd ed.
[5] O. Kistner and A. Sunyar, *Phys. Rev. Lett.* **4** (1960).
[6] H. Frauenfelder, *The Moessbauer Effect: A Review with a Collection of Reprints* (W.A. Benjamin, Inc., 1962).
[7] P. Bevington and D. Robinson, *Data Reduction and Error*

- Analysis for the Physical Sciences* (McGraw-Hill, 2003).
[8] S. DeBenedetti, G. Lang, and R. Ingalls, *Physical Review Letters* **6**, 60 (1961).

Acknowledgments

DVP gratefully acknowledges Brian Pepper's equal partnership, as well as the guidance and advice of Thomas Walker, Daniel Nezich and Scott Sewell.